27. J. E. M. Hornos *et al.*, *Phys. Rev. E* **72**, 051907 (2005).
28. Materials and methods are available as supporting material on *Science* Online.
29. We would like to thank G. Church, A. Miyawaki, and B. Wanner for bacterial strains and plasmids; J. Hearn for technical assistance; and J. Elf, N. Friedman, and G. W. Li for helpful discussions. This work was supported by the NIH Director's Pioneer Award. P.J.C. acknowledges the John and Fannie Hertz Foundation.

Supporting Online Material
www.sciencemag.org/cgi/content/full/322/5900/442/DC1
Materials and Methods
SOM Text
Figs. S1 to S8
Movie S1
References

5 June 2008; accepted 12 September 2008
10.1126/science.1161427

Remeasuring the Double Helix

Rebecca S. Mathew-Fenn,[1,2]* Rhiju Das,[2,3]*† Pehr A. B. Harbury[1,2]‡

DNA is thought to behave as a stiff elastic rod with respect to the ubiquitous mechanical deformations inherent to its biology. To test this model at short DNA lengths, we measured the mean and variance of end-to-end length for a series of DNA double helices in solution, using small-angle x-ray scattering interference between gold nanocrystal labels. In the absence of applied tension, DNA is at least one order of magnitude softer than measured by single-molecule stretching experiments. Further, the data rule out the conventional elastic rod model. The variance in end-to-end length follows a quadratic dependence on the number of base pairs rather than the expected linear dependence, indicating that DNA stretching is cooperative over more than two turns of the DNA double helix. Our observations support the idea of long-range allosteric communication through DNA structure.

Since the double helical structure of DNA was discovered 50 years ago (*1*), its average structure and internal fluctuations have been objects of intense study. Near its equilibrium structure, the DNA duplex is generally viewed as an ideal elastic rod. Current estimates put the bending rigidity B at ~230 pN·nm^2, the torsional rigidity C at 200 to 500 pN·nm^2, and the stretching modulus S (the extrapolated force required to double the length of the DNA) at ~1000 pN (*2*–*7*). Recent experimental observations, however, have called into question the accuracy of this simple mechanical picture. For example, single-molecule measurements show that overtwisting of DNA induces helix stretching (*8*). This twist-stretch coupling leads to a revised picture of DNA in which the helix core is modeled as an elastic rod while the phosphodiester backbone is modeled as a rigid wire. Analysis of DNA bending on short length scales has also yielded surprises. Specifically, ~100–base pair (bp) DNA helices circularize two to four orders of magnitude faster than would be predicted by the elastic rod model, leading to the idea that discrete kinks contribute to DNA bending (*9*, *10*).

The most straightforward way to characterize DNA structural fluctuations would be to directly visualize them under nonperturbing solution conditions. Kilobase-sized DNA structures have been imaged in real time, but it has not been possible to resolve bending, twisting, and stretching fluctuations at the microscopic level. Alternatively, analyzing the motions of very short DNA fragments simplifies the problem by limiting the contributions from bending. In practice, this has proved technically challenging. The experimental tools suited to the job, molecular rulers, provide an indirect readout of distance that is difficult to relate quantitatively to variation in end-to-end length. Indeed, short DNA duplexes are often assumed to be completely rigid and are used as length standard controls for new molecular rulers (*11*–*14*).

Our investigations apply a recently developed technique for measuring distance distribu-

[1]Biophysics Program, Stanford University, Stanford, CA 94305, USA. [2]Department of Biochemistry, Stanford University, Stanford, CA 94305, USA. [3]Department of Physics, Stanford University, Stanford, CA 94305, USA.
*These authors contributed equally to this work.
†Present address: Department of Biochemistry, University of Washington, Seattle, WA 98195, USA.
‡To whom correspondence should be addressed. E-mail: harbury@cmgm.stanford.edu

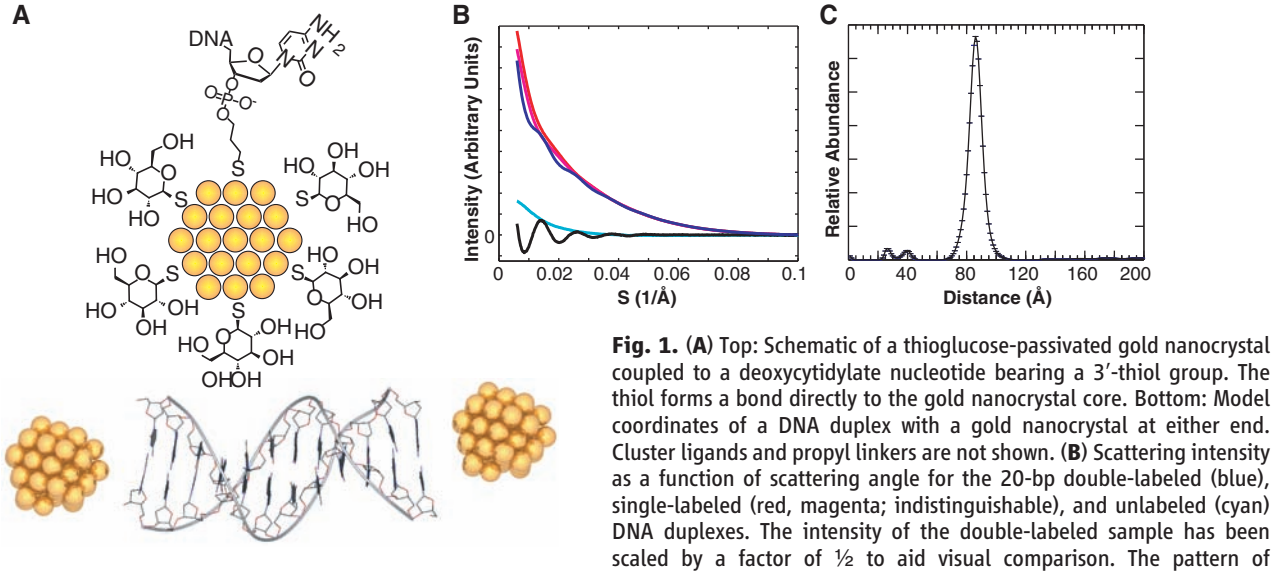

Fig. 1. (**A**) Top: Schematic of a thioglucose-passivated gold nanocrystal coupled to a deoxycytidylate nucleotide bearing a 3′-thiol group. The thiol forms a bond directly to the gold nanocrystal core. Bottom: Model coordinates of a DNA duplex with a gold nanocrystal at either end. Cluster ligands and propyl linkers are not shown. (**B**) Scattering intensity as a function of scattering angle for the 20-bp double-labeled (blue), single-labeled (red, magenta; indistinguishable), and unlabeled (cyan) DNA duplexes. The intensity of the double-labeled sample has been scaled by a factor of ½ to aid visual comparison. The pattern of scattering interference between the two nanocrystal labels (black) is obtained by summing the intensities of the double-labeled and unlabeled samples, then subtracting the intensities of the two single-labeled samples (*15*). The data were obtained at 200 μM DNA and are averages of 10 exposures of 1 s each. Measurements were made at 25°C in the presence of 70 mM Tris-HCl (pH 8.0), 100 mM NaCl, and 10 mM ascorbic acid. The scattering parameter S is defined as (2 sin θ)/λ, where 2θ is the scattering angle and λ is the x-ray wavelength. (**C**) Transformation of the nanocrystal scattering interference pattern into a weighted sum of sinusoidal basis functions (corresponding to different interprobe distances) yields the probability distribution for nanocrystal center-of-mass separation (*15*).

tions based on small-angle x-ray scattering interference between heavy-atom nanocrystals (*15*). Gold nanocrystals with radii of 7 Å are site-specifically attached to the ends of DNA double helices of varying length, as illustrated for a 20-bp DNA segment in Fig. 1A. The experimental scattering profile for this molecule (Fig. 1B) displays a characteristic oscillation with an inverse period of 86 Å, due to the scattering interference between the nanocrystals. This interference pattern is decomposed into a linear combination of basis scattering functions corresponding to discrete separation distances between the nanocrystals, providing the interparticle distance distribution (Fig. 1C). Distributions measured this way can be extremely sharp if the probes are at fixed distances, and they reveal broadened, highly skewed, or even bimodal distance distributions if they are present (*15*). The x-ray ruler reads out an effectively instantaneous distribution of distances, due to the short time scale of x-ray scattering from bound electrons. The nanocrystal labels produce no detectable disruption of the structure of DNA double helices (as monitored by circular dichroism spectroscopy) and negligibly alter the melting thermodynamics of the helices into single strands (table S1 and fig. S1). As a further precaution against any undetected effects on DNA structure from the gold probes, we base our conclusions below on the change in probe separation as the helix length is increased, and not on the absolute value of the measurement for a single DNA construct.

We prepared labeled DNA duplexes with lengths between 10 and 35 bp in 5-bp increments (table S2). The scattering interference profiles for these molecules (Fig. 2A) give end-to-end distance distributions with approximately symmetric fluctuations around a well-defined mean distance (Fig. 2B). The interprobe distance increases approximately linearly with the number of helix base pairs (Fig. 3A). A fit to these data that takes into account the potential displacement of the gold probes off of the helix axis (fig. S2) gives an average rise per base pair of 3.29 ± 0.07 Å (Fig. 3A), in close agreement with the average crystallographic value of 3.32 ± 0.19 Å (*16*). To estimate measurement errors, we compared distributions from independently prepared samples exposed at two different x-ray beamlines and with different detectors and calibration standards (fig. S3). The scatter in the mean was 0.4 Å for the shortest duplex and 0.9 Å for the longest duplex, with intermediate values for the other constructs (the error bars are smaller than the marker size in Fig. 3A). The deviation of the fit from the data exceeds the measurement error and may reflect sequence-dependent variation in the rise per base pair (*16*). The x-ray ruler gives a rise per base-pair intermediate between the lower values (2.9 to 3.1 Å) observed in microscopy experiments (*17*–*19*) and the somewhat higher "canonical"

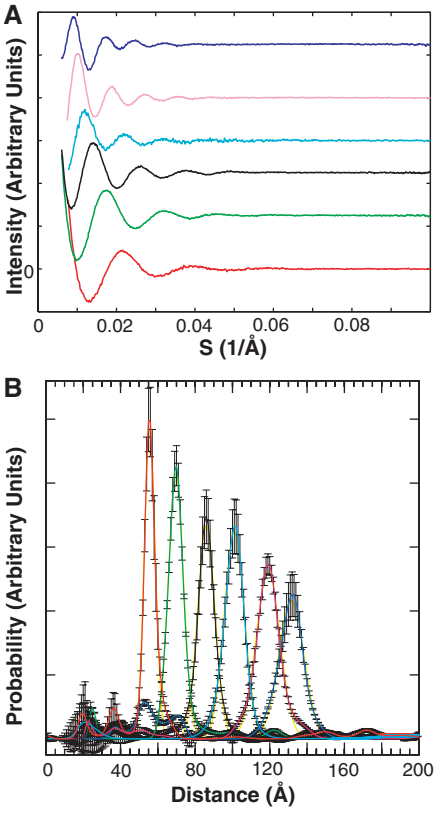

Fig. 2. (**A**) Nanocrystal scattering interference patterns obtained for the 10-bp (red), 15-bp (green), 20-bp (black), 25-bp (cyan), 30-bp (magenta), and 35-bp (blue) duplexes are offset vertically. See table S2 for DNA sequences. (**B**) Probability distance distribution curves for the 10-bp (red), 15-bp (green), 20-bp (black), 25-bp (cyan), 30-bp (magenta), and 35-bp (blue) duplexes. The distributions are normalized to sum to unity. Each distribution was fit to a Gaussian curve (yellow) using the "fminsearch" function in MATLAB. See fig. S10 for distance distribution curves plotted individually with error bars, and fig. S3 for repeated measurements using independently prepared samples at two different x-ray synchrotron beamlines.

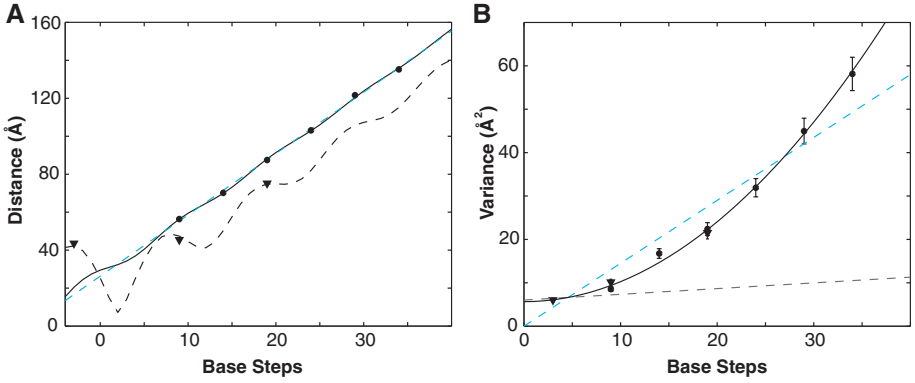

Fig. 3. (**A**) Mean nanocrystal-nanocrystal separation distance of end-labeled duplexes (circles) and internally labeled duplexes (triangles), plotted with respect to the number of intervening DNA base-pair steps. The distances for the end-labeled duplexes oscillate around a straight line (dashed blue line). A three-variable fit accounting for rotation of the nanocrystal probes around the helix axis (solid black line, fig. S2, $R^2 = 0.9995$) gives a rise per base pair of 3.29 ± 0.07 Å and a 9 Å radial displacement of the nanocrystals off of the helix axis. A similar two-variable fit to the internally labeled duplex distances (dashed black line, $R^2 = 0.9992$) gives a rise per base pair of 3.27 ± 0.1 Å and a 21 Å radial displacement of the nanocrystals off of the helical axis. Each fit takes into account the reduction in end-to-end length expected from bending fluctuations (table S3). The distance data points derive from the Gaussian curves in Fig. 2B. The measurement errors are estimated to be ±0.5%, according to repeat experiments with independently prepared samples at two different synchrotrons, and are smaller than the graph symbols (fig. S3). (**B**) Variance in nanocrystal-nanocrystal separation distance of end-labeled duplexes (circles) and internally labeled duplexes (triangles), plotted with respect to the number of intervening DNA base-pair steps. The variance predictions for an ideal elastic rod with a stretching modulus of 1000 pN (the value measured in single-molecule stretching experiments) are shown (dashed black line) and deviate grossly from the data. A linear relationship between variance and base-pair steps (dashed cyan line, two variables, $R^2 = 0.919$) is expected if the stretching of base-pair steps is uncorrelated along the DNA duplex (*24*). Alternatively, a quadratic relationship (solid black line, two variables, $R^2 = 0.997$) should hold if the DNA stretches cooperatively. The quadratic fit indicates that each base-pair step contributes 0.21 Å of standard deviation to the end-to-end length of a duplex. The y intercept of 5.7 Å^2 corresponds to variance arising from experimental factors. The variance data points derive from the Gaussian curves in Fig. 2B. Each fit takes into account the variance expected from bending fluctuations (table S3). The uncertainties in the variance values are estimated to be ±6.6%, based on the standard deviation of repeated measurements for the 25-bp duplex at independent beamlines and with independently prepared samples (fig. S3).

value (3.4 Å) obtained for DNA in condensed states or under tension (*20*, *21*).

Structural fluctuations of the DNA should be reflected in the width of the measured distance distributions after other sources of variance, such as linker flexibility and nanocrystal size heterogeneity, have been taken into account (Fig. 3B). DNA-independent factors are expected to contribute the same amount of variance to measurements with different duplexes (~6 $Å^2$ as fit in Fig. 3B). Thus, the increase in distribution width with DNA length must derive from structural changes in the DNA itself. Three facts argue that stretching fluctuations, rather than bending fluctuations or twisting fluctuations, dominate the approximately ±10% spread in end-to-end distance that we observe: (i) The DNA samples studied here are shorter than the bending persistence length of double-helical DNA (*22*). Both Monte Carlo calculations and an analytical approximation (table S3) (*23*) yield 7 $Å^2$ as the maximum contribution of bending fluctuations to the end-to-end length variance of the 35-bp duplex. This value accounts for only 14% of the observed variance. (ii) DNA bends produce asymmetrical distributions with shoulders at shorter distances (*15*), whereas the distributions we observe are symmetrical (Fig. 2B). (iiii) Because the nanocrystals lie close to the helical axis (Fig. 3A and fig. S2), twisting fluctuations have small effects on the measured end-to-end distances and cannot account for the observed variance.

The distance distributions are not consistent with the conventional model of the DNA duplex as an ideal elastic rod with a stretch modulus of ~1000 pN. To illustrate the point, suppose that the entire 8.5 $Å^2$ variance of the 10-bp duplex distribution arises from experimental sources unrelated to DNA stretching. Presumably, the same 8.5 $Å^2$ applies to the other duplex samples, which differ only by addition of base pairs to the center of the duplex sequence. The conventional model predicts that for the longest 35-bp duplex, DNA stretching should contribute an additional 3.3 $Å^2$ of variance, for a total variance of 11.8 $Å^2$ (dashed black line in Fig. 3B) (*24*). In fact, the observed variance is 51 $Å^2$; the contribution of DNA stretching to the variance is larger than predicted by a factor of ~13. A linear fit of the observed variances with respect to DNA length (dashed cyan line in Fig. 3B) indicates an apparent stretch modulus of ~91 pN. The resistance of DNA to stretching is thus weaker in the absence of tension, as measured herein, than in the presence of high tension, as in single-molecule stretching experiments.

A notable feature of the x-ray scattering data is the change in variance with duplex length (Fig. 3B). The elastic rod model predicts that the variance should increase linearly with the number of base steps (dashed lines in Fig. 3B). In contrast, we observe a quadratic dependence of variance on DNA length. The errors in the measured variances fall between 0.2 and 2.0 $Å^2$, according to replicate measurements at different x-ray beamlines with independently prepared samples (fig. S3). The data fit a quadratic dependence to within this measurement error (black line; $\chi^2 = 7.5$ with 7 degrees of freedom; $P = 0.39$), but not a linear dependence (cyan dashed line; $\chi^2 = 91$ with 7 degrees of freedom; $P = 7.4 \times 10^{-17}$). A quadratic increase in variance can only occur if the stretching fluctuations of neighboring base steps in a duplex are tightly correlated (*24*). Fits to models that interpolate between linear and quadratic dependences with a range of correlation lengths are given in fig. S4. These fits demonstrate that the stretching correlation must persist over at least two turns of a double helix. Thus, short DNA fragments stretch cooperatively: As the first two bases move farther apart, so do the last two bases.

We performed numerous controls to rule out experimental artifacts. One worry was that the nanocrystals or DNA might be damaged by x-ray radiation. A variety of tests showed that, in the presence of the radical scavenger ascorbate, the samples were not damaged during data collection (fig. S5) (*15*). Another concern was that as the synthetic DNA fragments became longer, the incidence of single base deletions might increase, resulting in an anomalous length-variance trend. However, electrophoretic and chromatographic analyses showed that all of the samples were >94% pure (figs. S5 and S6). A third possibility was that a lower signal-to-noise ratio in the longer-duplex data sets might lead to broadened distributions. However, when all of the data sets were degraded by truncation at low scattering angles and by addition of white noise so as to match the 35-bp data set, the measured means and variances did not change appreciably (fig. S7). To control for possible end effects, three duplexes were labeled internally by attaching gold probes to the DNA bases (fig. S8). The distance measurements for these internally labeled duplexes were consistent with the measurements for the end-labeled duplexes (Fig. 3).

Finally, we examined how long-range electrostatic forces might affect the end-to-end distance distributions. The nanocrystals prepared for these studies possess a weak net negative charge (as assessed by gel electrophoresis). Nonetheless, measurements at 10 mM, 100 mM, and 1 M NaCl (Debye screening lengths of 30 Å, 10 Å, and 3 Å, respectively) gave indistinguishable variances, indicating a negligible role of electrostatic repulsion between the two probes and between the probe and DNA in the variance measurements. The melting temperatures for the unlabeled, singly labeled, and doubly labeled duplexes also indicated a negligible interaction energy between the nanocrystals (table S1).

In light of our findings, we reexamined previous structural studies of short DNA duplexes (*24*). A comprehensive analysis of the end-to-end lengths for DNA duplexes in the Nucleic Acid Database reveals a range of distances that is consistent with our solution observations (fig. S9). However, this crystallographic distribution might be artificially broadened because it includes many different DNA sequences and crystallization conditions, or artificially narrowed because it includes many structures solved at 109 K. A plot of crystallographic length variance with respect to number of base steps is noisy and can be fit equally well with linear or quadratic curves. These data are therefore inconclusive with respect to the cooperativity of DNA stretching. We also reevaluated recently published time-resolved single-molecule fluorescence resonance energy transfer (FRET) (*25*) and electron spin resonance data (*26*) measured on DNA duplex samples. Plots of the end-to-end length variance derived from these data with respect to duplex length are clearly better fit by a quadratic relationship than by a linear relationship (fig. S9; both fits have 2 degrees of freedom). Although the data are noisy, the independent molecular-ruler measurements support the conclusion that short DNA duplexes stretch cooperatively.

A remaining puzzle is why DNA under tension appears to be much stiffer than relaxed DNA. One possibility is that the soft stretching mechanism we observe has a limited range and is fully extended at tensions greater than ~10 pN (the force above which helix stiffness is

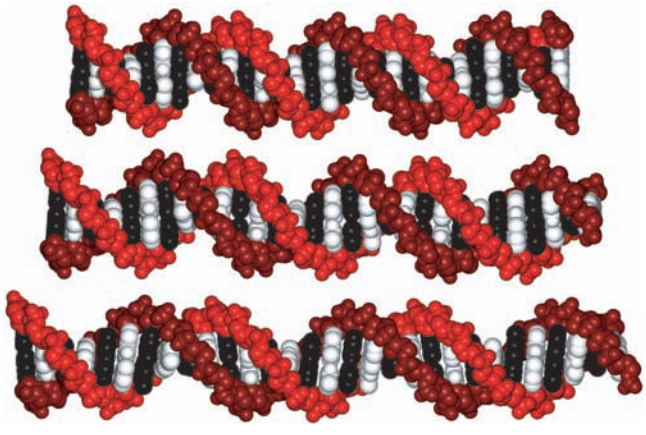

Fig. 4. Molecular models of 30-bp B-form DNA double helices with lengths 10% smaller (top) and 10% larger (bottom) than the canonical length (center) preserve base pairing geometry and are sterically allowed. The models were produced using Rosetta with constraints on local rise parameters to induce compression or stretching (*30*). The starting model coordinates were generated by the DNA Star Web Server (*31*). The figure was rendered with PovScript+ (*32*).

typically measured in single-molecule force-extension curves). For example, suppose that each base step can adopt either a short or a long conformation (say 3.3 Å ± 10%) of equivalent energy, and that the conformational state of contiguous bases is correlated over a length of 35 nucleotides. In the absence of tension, short DNA duplexes would populate equally the short and long conformations and therefore exhibit end-to-end distance distributions covering ±10% of the mean length (Fig. 4). The variance of these distributions would grow quadratically with duplex length (*24*). Under a stretching force, however, the DNA would preferentially adopt the long conformation, and this degree of freedom would saturate at modest tensions. At room temperature, 99% of the base steps would exist in the long conformation under 8 pN of applied force, and the apparent stretching modulus would be 1000 pN (*24*). Thus, a very soft stretching degree of freedom in the absence of tension can behave as a very stiff stretching degree of freedom when the duplex is under tension. The stretching of DNA at larger forces would presumably occur by a different mechanism. We note that this two-state model is oversimplified with respect to our data because our measurements would spatially resolve the short and long states if only two existed. However, the saturation behavior holds for models with a larger number of states.

Additional theoretical and experimental work will be required to reveal the microscopic basis for correlated DNA stretching fluctuations and its potential relation to other recently discovered nonideal properties of DNA (*8*–*10*). Whereas FRET experiments with nanosecond time resolution indicate large DNA stretching fluctuations (*25*), alternative FRET experiments that average single-molecule FRET signals over hundreds of microseconds do not (*27*). Thus, DNA stretching dynamics likely occur on a time scale between 10^{-8} and 10^{-5} s. Molecular simulations intended to model DNA stretching will have to access this time regime.

The presence of long-range stretching correlations implies that DNA double helices can, in principle, transmit information over at least 20 bp through an allosteric "domino effect" (*28*, *29*). For example, in the context of the two-state model, a protein that favors binding to a stretched segment of double helix would disfavor the binding of another protein that prefers a compressed conformation. This effect would propagate to sites within 20 bp, and possibly farther. Whether such DNA-mediated allosteric communication alters how the double helix and its specific binding partners interact to regulate biological processes remains to be tested.

References and Notes

1. J. D. Watson, F. H. Crick, *Nature* **171**, 737 (1953).
2. Z. Bryant *et al.*, *Nature* **424**, 338 (2003).
3. S. B. Smith, Y. Cui, C. Bustamante, *Science* **271**, 795 (1996).
4. D. Shore, R. L. Baldwin, *J. Mol. Biol.* **170**, 957 (1983).
5. D. Shore, R. L. Baldwin, *J. Mol. Biol.* **170**, 983 (1983).
6. M. D. Wang, H. Yin, R. Landick, J. Gelles, S. M. Block, *Biophys. J.* **72**, 1335 (1997).
7. D. E. Depew, J. C. Wang, *Proc. Natl. Acad. Sci. U.S.A.* **72**, 4275 (1975).
8. J. Gore *et al.*, *Nature* **442**, 836 (2006).
9. T. E. Cloutier, J. Widom, *Mol. Cell* **14**, 355 (2004).
10. T. E. Cloutier, J. Widom, *Proc. Natl. Acad. Sci. U.S.A.* **102**, 3645 (2005).
11. A. Hillisch, M. Lorenz, S. Diekmann, *Curr. Opin. Struct. Biol.* **11**, 201 (2001).
12. C. Sönnichsen, B. M. Reinhard, J. Liphardt, A. P. Alivisatos, *Nat. Biotechnol.* **23**, 741 (2005).
13. P. Zhu, J. P. Clamme, A. A. Deniz, *Biophys. J.* **89**, L37 (2005).
14. L. S. Churchman, Z. Okten, R. S. Rock, J. F. Dawson, J. A. Spudich, *Proc. Natl. Acad. Sci. U.S.A.* **102**, 1419 (2005).
15. P. A. B. Harbury, *PLoS ONE* **3**, e3229 (2008).
16. W. K. Olson, A. A. Gorin, X. J. Lu, L. M. Hock, V. B. Zhurkin, *Proc. Natl. Acad. Sci. U.S.A.* **95**, 11163 (1998).
17. J. D. Griffith, *Science* **201**, 525 (1978).
18. C. Rivetti, M. Guthold, C. Bustamante, *J. Mol. Biol.* **264**, 919 (1996).
19. K. Sakata-Sogawa, M. Kurachi, K. Sogawa, Y. Fujii-Kuriyama, H. Tashiro, *Eur. Biophys. J.* **27**, 55 (1998).
20. S. B. Zimmerman, B. H. Pheiffer, *J. Mol. Biol.* **135**, 1023 (1979).
21. N. B. Ulyanov, T. L. James, *Methods Enzymol.* **261**, 90 (1995).
22. C. G. Baumann, S. B. Smith, V. A. Bloomfield, C. Bustamante, *Proc. Natl. Acad. Sci. U.S.A.* **94**, 6185 (1997).
23. J. M. Schurr, B. S. Fujimoto, *Biopolymers* **54**, 561 (2000).
24. See supporting material on *Science* Online.
25. T. A. Laurence, X. Kong, M. Jager, S. Weiss, *Proc. Natl. Acad. Sci. U.S.A.* **102**, 17348 (2005).
26. Q. Cai *et al.*, *Nucleic Acids Res.* **34**, 4722 (2006).
27. E. Nir *et al.*, *J. Phys. Chem. B* **110**, 22103 (2006).
28. J. M. Schurr, J. J. Delrow, B. S. Fujimoto, A. S. Benight, *Biopolymers* **44**, 283 (1997).
29. K. M. Kosikov, A. A. Gorin, V. B. Zhurkin, W. K. Olson, *J. Mol. Biol.* **289**, 1301 (1999).
30. A. V. Morozov, J. J. Havranek, D. Baker, E. D. Siggia, *Nucleic Acids Res.* **33**, 5781 (2005).
31. Y. Liu, D. L. Beveridge, *J. Biomol. Struct. Dyn.* **18**, 505 (2001).
32. T. D. Fenn, D. Ringe, G. A. Petsko, *J. Appl. Crystallogr.* **36**, 944 (2003).

33. We thank C. J. Ackerson for discussions on nanocrystal synthesis; R. L. Baldwin, F. E. Boas, Z. D. Bryant, L. S. Churchman, A. R. Dunn, D. R. Halpin, D. Herschlag, W. L. Martin, B. H. Robinson, J. M. Schurr, A. L. Smith, R. M. Weisinger, and S. J. Wrenn for insights into DNA; Y. Bai, S. Doniach, K. Ito, J. Lipfert, I. S. Millett, S. Seifert, P. Thiyagarajan and H. Tsuruta for assistance and advice on x-ray scattering; T. D. Fenn for writing code that was used to calculate crystallographic dispersion values and for valuable discussions throughout this work; P. A. Walker for expert assistance with DNA synthesis; and P. Bradley and D. Baker for permitting use of unpublished code to prepare Fig. 4. Supported by NIH grants GM068126-01 and DP OD000429-01 (P.A.B.H.), an NIH training grant fellowship (R.S.F.), an NSF graduate fellowship (R.D.), and the U.S. Department of Energy (contract W-31-109 Eng-438 to the Advanced Photon Source, and support of Stanford Synchrotron Radiation Laboratory).

Supporting Online Material

www.sciencemag.org/cgi/content/full/322/5900/446/DC1
Materials and Methods
SOM Text
Figs. S1 to S10
Tables S1 to S4
References

9 April 2008; accepted 3 September 2008
10.1126/science.1158881

Relation Between Obesity and Blunted Striatal Response to Food Is Moderated by *Taq*IA A1 Allele

E. Stice,[1,2]* S. Spoor,[1] C. Bohon,[1,3] D. M. Small[4,5]

The dorsal striatum plays a role in consummatory food reward, and striatal dopamine receptors are reduced in obese individuals, relative to lean individuals, which suggests that the striatum and dopaminergic signaling in the striatum may contribute to the development of obesity. Thus, we tested whether striatal activation in response to food intake is related to current and future increases in body mass and whether these relations are moderated by the presence of the A1 allele of the *Taq*IA restriction fragment length polymorphism, which is associated with dopamine D2 receptor (*DRD2*) gene binding in the striatum and compromised striatal dopamine signaling. Cross-sectional and prospective data from two functional magnetic resonance imaging studies support these hypotheses, which implies that individuals may overeat to compensate for a hypofunctioning dorsal striatum, particularly those with genetic polymorphisms thought to attenuate dopamine signaling in this region.

Although twin studies suggest that biological factors play a major role in the etiology of obesity, few prospective studies have identified biological factors that increase risk for future weight gain. Dopamine is involved in the reinforcing effects of food (*1*). Feeding is associated with dopamine release in the dorsal striatum, and the degree of pleasure from eating correlates with amount of dopamine release (*2*, *3*). The dorsal striatum responds to

www.sciencemag.org/cgi/content/full/322/5900/446/DC1

Supporting Online Material for

Remeasuring the Double Helix

Rebecca S. Mathew-Fenn, Rhiju Das, Pehr A. B. Harbury*

*To whom correspondence should be addressed. E-mail: harbury@cmgm.stanford.edu

Published 17 October 2008, *Science* **322**, 446 (2008)
DOI: 10.1126/science.1158881

This PDF file includes:

Materials and Methods:

Synthesis and purification of oligonucleotides:

The DNA sequences used in this study are reported in Supplemental Table S1. All oligonucleotides were prepared on an automated ABI 394 DNA synthesizer (Applied Biosystems) and retained a 5'-dimethoxytrityl (DMT) group when cleaved from the resin. Thiols were incorporated into the end-labeled oligonucleotides using the Glen Research C3 thiol modifier (part # 20-2933-41). Amino-allyl dT was incorporated into internal-labeled oligonucleotides using the Glen Research amino C2 dT modifier (part # 10-1037-90). Following deprotection in concentrated ammonium hydroxide, the oligonucleotides were purified by HPLC as previously described (*S1*). Full-length product fractions were concentrated ten-fold by centrifugal evaporation. DMT groups at the 5'-terminus were removed by addition of trifluoroacetic acid. The oligonucleotides were then immediately precipitated by addition of 10 mM magnesium chloride and five volumes of ethanol.

The internally labeled oligonucleotides were derivatized at amino-allyl dT positions using succinimidyl 3-(2-pyridyldithio)propionate (SPDP) (Invitrogen #S-1531). A solution containing 20 nmols of the amino-allyl dT oligonucleotide was dissolved in 250 μL of 0.1 M borate buffer at pH 8.5. SPDP (5 mg) dissolved in 250 μL of dimethylformamide was then added and the reaction mixture was incubated for six hours at room temperature. SPDP-modified oligonucleotides were separated from starting materials by reverse-phase HPLC (Zorbax Eclipse XDB-C18) with a linear gradient from 0 to 90% acetonitrile in 0.1 M triethylammonium acetate, pH 5.5. The product fractions were concentrated ten-fold by centrifugal evaporation. Just prior to gold coupling

reactions, the resuspended SPDP-modified oligonucleotides were treated with 100 mM dithiothreitol (DTT) for 30 minutes at 70°C to reduce the internal disulfide bond. Excess DTT was removed by transferring the solution to a fresh tube, followed by a second ethanol precipitation step, as above.

Coupling of gold nanocrystals to oligonucleotides:

Thioglucose-passivated gold nanocrystals were synthesized and purified as previously described (*S1*). Gold nanocrystals were coupled to single-stranded DNA (ssDNA) by mixing 60 nmols of thiol-modified DNA oligonucleotide with a five-fold molar excess of gold nanocrystals in 100 µL of 100 mM tris-HCl, pH 9.0, for two hours at room temperature. The gold-ssDNA conjugates were purified by ion-exchange HPLC, and incubated with an appropriate complementary ssDNA for 30 minutes at room temperature. The desired double-stranded DNA (dsDNA) was purified by ion-exchange HPLC, and subsequently desalted and concentrated.

X-ray scattering:

Small-angle X-ray scattering experiments were performed at the BESSRC-CAT beamline 12-ID of the Advanced Photon Source (APS) and at beamline 4-2 of the Stanford Synchrotron Radiation Lab (SSRL). See Mathew-Fenn and colleagues (*S1*) for a more detailed description of the data acquisition and analysis procedures.

Capillary electrophoresis:

Capillary electrophoresis analysis of sense-strand thiol-modified ssDNA oligonucleotides was performed using the Beckman P/ACE Molecular Characterization

System (Beckman Coulter Inc., Fullerton, CA), equipped with a 45 cm, 100 µm inner diameter, 375 µm outer diameter neutral capillary (Part # 477477, Beckman Coulter Inc., Fullerton, CA) and a glass syringe pump. The separation media consisted of a linear polyacrylamide gel (Part # 477621, Beckman Coulter Inc., Fullerton, CA) dissolved in running buffer (Part # 338481, Beckman Coulter Inc., Fullerton, CA). The running buffer contained 7 M urea to prevent secondary structure formation. The ssDNA 100-R test mix (Part # 477626, Beckman Coulter Inc., Fullerton, CA) was used to evaluate sizing accuracy for these results. Each ssDNA sample was diluted in deionized water to a final concentration of 10 µg/mL, heated to 95° C for 2 minutes and cooled on ice. Samples were injected into the capillary tube from the cathodic end by positive pressure. Electrophoresis was conducted with a reversed-polarity constant voltage of 11.4 kV for 30 minutes. Eluting ssDNA was detected by absorbance at 254 nm.

Determination of crystallographic variances:

Olson and colleagues (*S2*) previously determined average rise and dispersion values for dimer steps taken from 70 naked B-form DNA coordinate files. A search of the current nucleic acid database (*S3*) yielded an additional 100 naked B-form DNA coordinate sets. All 170 coordinate files were used to calculate rise and dispersion values for step sizes ranging from 2-10 (see Appendix C for a complete list of the coordinate files). Base-step separation distances were measured from the terminal oxygen on the phosphate backbone on the sense strand (O5') to the terminal oxygen on the complementary strand (O5').

Distance distributions from published time-resolved smFRET data:

Laurence and colleagues (*S4*) report the first and second moment (mean $\hat{E}$ and standard deviation σ_E) for the efficiency distribution of fluorescence resonance energy transfer between donor and acceptor fluorophores coupled to DNA duplexes. The efficiencies are derived from time-resolved single-molecule FRET measurements that differentiate between states in slow exchange on the nanosecond timescale. The authors do not transform their data into distance distributions. We performed this transformation based on the assumption that the efficiency distributions, *dP(E)*, are Gaussian:

$$dP(E) = \sqrt{\frac{1}{2\pi\sigma_E^2}} e^{-\left(E-\hat{E}\right)^2/\left(2\sigma_E^2\right)} dE$$

We also assumed that the Förster expression for the relationship between transfer efficiency and inter-probe distance, *L*, was applicable:

$$E(L) = \left\{1 + \left(L/R_0\right)^6\right\}^{-1}$$

where R_0 is the Förster distance. Given these assumptions, distance probability distributions, *dP(L)*, were computed as:

$$\frac{dP(L)}{dL} = \int_{E(L+dL/2)}^{E(L-dL/2)} \frac{dP(E)}{dE} dE \approx \frac{dP(E(L))}{dE}\left[E\left(L - dL/2\right) - E(L + dL/2)\right]$$

The data from Laurence and co-workers included eight samples with a tetramethylrhodamine donor fluorophore and an Alexa 647 acceptor fluorophore:

Base Steps	Donor	Acceptor	$\hat{E}$	σ_E
5	Internal	Internal	0.909	0.051
7	End	Internal	0.958	0.0214
12	End	Internal	0.8	0.14
15	Internal	Internal	0.604	0.208

17	End	Internal	0.56	0.205
22	End	Internal	0.32	0.225
25	Internal	Internal	0.122	0.077
27	End	Internal	0.16	0.145

We used the value of the Förster distance (R_0=69Å) that was measured by the authors (*S4*).

Appendix A:

Length distributions from the linear elastic rod model. The linear elastic rod model assumes that DNA, when stretched or compressed away from its unperturbed length L_0, will generate a restoring force (F) that increases linearly with the fractional extension (X_f):

$$F = -SX_f \text{ where } X_f = (L - L_0)/L_0$$

L denotes the perturbed length of the DNA, and the linear coefficient S is called the stretch modulus. Integrating the product of force and distance gives the energy [$E(L)$] of the DNA as a function of its length:

$$E(L) = \frac{S}{2L_0}(L - L_0)^2$$

Insertion of this energy into Boltzman's law gives the relative probability $dP(L)$ that the DNA will adopt the length L:

$$dP(L) = \sqrt{\frac{S}{2\pi L_0 RT}} e^{-S(L-L_0)^2/(2L_0RT)} dL$$

This probability distribution is Gaussian with mean length L_0 and variance $\sigma^2 = L_0RT/S$. One can thus infer an apparent force modulus from a Gaussian end-to-end distribution as $S_{apparent} = L_0RT/\sigma^2$. Alternatively, if L_0 is expressed as a product of the number of base pairs, N, and the mean rise per base-pair, $\hat{r}$ (specifically $L_0 = N\hat{r}$), then the end-to-end length variance for different sizes of duplexes can be written $\sigma^2 = N\hat{r}RT/S$. In plots of end-to-end length variance with respect to number of base pairs, the slope (m) of a linear fit will be $m = \hat{r}RT/S$. By rearrangement, this slope yields an apparent force modulus: $S_{apparent} = \hat{r}RT/m$ (the apparent force modulus cited in the text was calculated this way). In force-extension units, $RT \approx 4$ pN•nm at 25°C.

Appendix B:

Length variance of DNA duplexes. Consider a DNA duplex made up of N equivalent DNA base-pair steps (the steps will be indexed with the subscript i). Suppose that each of the individual steps can populate multiple different conformations characterized by different values of the rise per base-pair (r). Because of equivalence, all of the steps should exhibit the same mean rise ($\hat{r}$) and the same variance of rise σ^2_{step}:

$$\langle r_i \rangle = \hat{r} \text{ and } \left\langle (r_i - \hat{r})^2 \right\rangle = \sigma^2_{step} \text{ for all } i=1...N$$

The length of the duplex, L, is the sum of the rises for the individual base-pair steps: $L = \sum_{i=1...N} r_i$. This length will fluctuate around the mean length $L_0 = N\hat{r}$. The end-to-end length variance of the duplex, σ^2_{duplex}, can then be expressed in terms of the properties of the individual base-pair steps:

$$\sigma^2_{duplex} = \left\langle (L - L_0)^2 \right\rangle = \left\langle \left([r_1 - \hat{r}] + ... + [r_N - \hat{r}] \right)^2 \right\rangle = \sum_{i=1...N} \left\langle (r_i - \hat{r})^2 \right\rangle + \sum_{\substack{i=1...N,\, j=1...N \\ i \neq j}} \left\langle (r_i - \hat{r})(r_j - \hat{r}) \right\rangle$$

$$= N\sigma^2_{step} + (N^2 - N)\overline{\left\langle (r_i - \hat{r})(r_j - \hat{r}) \right\rangle}$$

The over-bar in the final expression denotes an average over all i and j with $i \neq j$. If the rise fluctuations of individual base-pair steps are completely uncorrelated with each other, then the right term evaluates to zero and $\sigma^2_{duplex} = N\sigma^2_{step}$: a linear increase in length variance with increase in number of base pairs N. Alternatively, if the fluctuations of all of the base-pair steps are fully correlated, then the right term evaluates to $(N^2 - N)\sigma^2_{step}$ and $\sigma^2_{duplex} = N^2\sigma^2_{step}$: a quadratic increase in length variance with increase in number of

base pairs *N*. This conclusion does not depend on the nature of the underlying distribution of rise for the individual base-pair steps.

Length variance with partial correlation. Suppose that the fluctuations of the *N* base-pair steps described above are only partially correlated. For example, suppose that the correlation in rise fluctuations falls off exponentially with the separation between two base-pair steps:

$$\left\langle (r_i - \hat{r})(r_j - \hat{r}) \right\rangle = \sigma_{step}^2 e^{-|i-j|/\xi}$$

Here, ξ is a correlation length related to the energetic cost, $E_{boundary} = RT \ln[\xi]$, of a transition boundary between different rise conformations. If only two alternate rise conformations exist (see below), the model is identical to the one-dimensional Ising model. The end-to-end length variance of the duplex, σ_{duplex}^2, can be expressed in terms of the properties of the individual base-pair steps as:

$$\sigma_{duplex}^2 = \left\langle (L - L_0)^2 \right\rangle = \left\langle \left([r_1 - \hat{r}] + ... + [r_N - \hat{r}] \right)^2 \right\rangle = \sum_{\substack{i=1...N \\ j=1...N}} \left\langle (r_i - \hat{r})(r_j - \hat{r}) \right\rangle$$

$$\approx 2 \int_{i=1}^{N} \int_{j=i}^{N} \sigma_{step}^2 e^{-|i-j|/\xi} \, didj = 2\sigma_{step}^2 \xi \int_{i=1}^{N} \left[1 - e^{-(N-i)/\xi} \right] di = 2\sigma_{step}^2 \xi \left[N - \xi \left(1 - e^{-N/\xi} \right) \right]$$

When the duplex is much shorter than the correlation length ($N \ll \xi$) the variance simplifies to $\sigma_{duplex}^2 = N^2 \sigma_{step}^2$. Alternatively, when the duplex is much longer than the correlation length ($N \gg \xi$), the variance simplifies to $\sigma_{duplex}^2 = 2\sigma_{step}^2 \xi N$. In Fig. S4, we fit this partial correlation model to our variance data assuming different values for the correlation length ξ.

Force-extension curves for a simplified model with two values of rise. Consider a DNA duplex made up of N equivalent base-pair steps. Suppose that each base-pair step can adopt two different conformations of equivalent energy: a short conformation with a rise of l_0-Δ and a long conformation with a rise of l_0+Δ. Also suppose that the conformations of the base-pair steps in the duplex are fully correlated: the duplex is either all short or all long. In the absence of a perturbation, the duplex will populate the short and long conformations equally, producing a mean length L_0=Nl_0. If a stretching force F is applied to the ends of the duplex, the long state will be stabilized by $FN\Delta$ and the short state will be destabilized by the same amount. Using Boltzman's law, the population likelihood P_{long}/P_{short} of the long/short state will become:

$$P_{long} = \frac{e^{FN\Delta/(RT)}}{e^{FN\Delta/(RT)} + e^{-FN\Delta/(RT)}} \text{ and } P_{short} = \frac{e^{-FN\Delta/(RT)}}{e^{FN\Delta/(RT)} + e^{-FN\Delta/(RT)}}$$

The average length L of the duplex as a function of applied force can then be computed:

$$L = L_0 + N\Delta P_{long} - N\Delta P_{short} = L_0 + \frac{N\Delta e^{FN\Delta/(RT)} - N\Delta e^{-FN\Delta/(RT)}}{e^{FN\Delta/(RT)} + e^{-FN\Delta/(RT)}}$$

and the fractional extension $X_f = (L - L_0)/L_0$ as:

$$X_f = \frac{N\Delta}{L_0}\left(\frac{e^{FN\Delta/(RT)} - e^{-FN\Delta/(RT)}}{e^{FN\Delta/(RT)} + e^{-FN\Delta/(RT)}}\right) = \frac{N\Delta}{L_0}\tanh\left[\frac{FN\Delta}{RT}\right]$$

If we define the apparent force modulus, $S_{apparent}$, to be the slope of the force-fractional extension curve ($S_{apparent} = \frac{\partial F}{\partial X_f}$), then:

$$S_{apparent} = \frac{L_0 RT}{N^2\Delta^2}\cosh^2\left[\frac{FN\Delta}{RT}\right]$$

Taking N=35, l_0=0.34 nm per base, Δ=0.1*l_0=0.034 nm, and F=8 pN, P_{long} evaluates to 0.99 (the duplex spends 99% of the time in the long state), and $S_{apparent}$ evaluates to 1000

pN (the apparent force modulus for stretching via this mechanism). Thus, a very soft stretching degree of freedom in the absence of tension can behave as a very stiff stretching degree of freedom when the duplex is under tension. This model is oversimplified with respect to our data because we would have been able to spatially resolve different correlated rise states if only two existed. However, the basic behavior derived above holds for models with a larger number of rise states.

Supplementary Figure Captions:

Fig. S1. Nanocrystal probes do not alter the structure of duplex DNA as measured by circular dichroism (CD) spectra. Twelve spectra are shown, corresponding to the unlabeled and double-labeled forms of the 10, 15, 20, 25, 30 and 35 base-pair DNA duplexes. The CD spectrum of a 500 basepair RNA duplex (black) is also shown to illustrate the differences in CD signal between A-form and B-form nucleic-acid helices.

Fig. S2: Geometric model of the double helix used to fit distance data. [A] Cartoon of a double helix (rendered using PovScript$^+$ (*S5*)) labeled with two gold nanocrystals (black balls). The distance between the two probes *L*, as a function of the number of intervening base steps *N*, was fit as the Pythagorean sum of the axial and radial separation distances:

$$L(N) = \sqrt{axial^2 + radial^2} = \sqrt{\left(axial_0 + rN\right)^2 + \left(2D\sin\left[\left(\theta_0 + \frac{2\pi}{10.4}N\right)/2\right]\right)^2}$$

The fit parameters were *r*, the axial rise per base step, and *D*, the radial displacement of the probes off of the helical axis. The term $axial_0$ is the axial distance between two probes separated by zero base steps. The term θ_0 is the azimuthal angle between two probes separated by zero base steps. [B] The labeled duplex viewed in projection along the helix axis with θ denoting the azimuthal angle between the probes. The radial separation distance was calculated as $radial = 2D\sin[\theta/2]$. The azimuthal angle as a function of base steps was calculated $\theta = \theta_0 + 2\pi N/10.4$. The constant in the denominator derives from the fact that 10.4 base pairs of DNA in solution make one full turn around the helix axis. Values for θ_0 were determined by inspection of the Dickerson dodecamer structure. For probe attachment to 3'-phosphates (end labels), θ_0 was set to 1.34π. For probe attachment to the exocyclic methyl groups of T bases (internal labels), θ_0 was set to 1.58π. [C] Two gold nanocrystals separated by zero base steps. The nanocrystals are attached at terminal 3'-phosphate positions of an A:T base pair through three-atom linkers. The axial separation between the nanocrystals corresponds to the parameter $axial_0$. For the end-labeled samples, $axial_0$ was fit to the data, and it optimized to a value of 24 Å. The figure also shows the amino-allyl/SPDP modification of the T base that was used to attach nanocrystals at internal positions of a duplex. For the internally-labeled samples, $axial_0$ was assumed to be zero.

Fig. S3: Repeat measurement of distance distributions using independently prepared samples and two different synchrotron X-ray sources. Data for the 10 [A], 25 [B], and 35 [C] base-pair duplexes are shown. Independent samples are labeled A and B followed by the month/year in which they were prepared. The plot key also indicates the synchrotron source (SSRL - Stanford Synchrotron Radiation Laboratory, APS - Advanced Photon Source) followed by the month/year in which the data were collected. The mean and variance of a Gaussian fit to each distribution is reported. The dominant distribution feature for each duplex is extremely reproducible. The small distribution features are variable and appear to correlate with sample preparation and freezer storage time (see sample A in panel A).

Fig. S4: Fits of experimental variance data to a duplex model with partial correlation (Appendix B). Values for the correlation length ξ are 10 base steps [red: χ^2 = 25.24, seven degrees of freedom; P = 0.0007], 20 base steps [black: χ^2 = 12.56; P = 0.084] and 80 base steps [blue: χ^2 = 7.29; P = 0.40]. For each correlation length, optimum values of σ^2_{step} and of the y-intercept were fit to the data.

Fig. S5: Purification of nanocrystal-labeled DNA. [A] Ion-exchange HPLC chromatogram of a reaction mixture containing uncoupled gold nanocrystals (Au), a 25 base ssDNA-gold conjugate ($Au_{25}S$), and gold nanocrystals coupled to multiple ssDNA strands (Au_{25}*). [B] Ion-exchange HPLC chromatogram of a 25 base pair dsDNA-gold conjugate ($Au_{25}D$). The purification step after formation of duplexes eliminates excess ssDNA, and gold nanocrystals coupled to multiple dsDNA's (Au_{25}*). [C] Ion-exchange HPLC chromatogram of a purified 25 base-pair dsDNA-gold conjugate ($Au_{25}D$) after desalting, concentration to 200 μM, and storage at -20 ºC for 14 days. [D] Ion-exchange HPLC chromatogram of a 25 base-pair dsDNA-gold conjugate sample ($Au_{25}D$) after exposure to X-ray radiation during data collection.

Fig. S6: Oligonucleotide purity. Capillary electropherograms are shown for the 10 [A, 96%], 15 [B, 96%], 20 [C, 96%], 25 [D, 95%], 30 [E, 94%], and 35 [F, 99%] sense-strand, thiol-modified DNA oligonucleotides.

Fig. S7: Effect of reduced signal-to-noise on distance distributions. [A] Nanocrystal scattering interference data for the 10 (red), 15 (green), and 20 (black) base-pair duplex samples were truncated at low values of S, and degraded by addition of white noise, so as to match the signal characteristics of the scattering interference data from the 35 base-pair duplex (blue). Figure 2a of the manuscript shows the original interference patterns. [B-D] Probe center-of-mass distance probability distributions for the 10 [B], 15 [C] and 20 [C] base-pair duplexes computed using the scattering interference data in [A]. The mean and variance of Gaussian fits to the full data sets (supplemental Fig. 1) are titled "Full Data:". The mean and variance of Gaussian fits to the truncated data sets (blue solid lines) are titled "Truncated:".

Fig. S8: Distance distributions for internally labeled DNA duplexes. [A] Nanocrystal scattering interference curves measured for internally labeled duplexes with probe separations of 3 [red], 9 [cyan], and 19 [black] base steps. The data sets are offset vertically. [B-D] Probe center-of-mass distance probability distributions for duplexes with probe separations of 3 [B], 9 [C], and 19 [D] base steps. The distributions are normalized so that they sum to unity. Error bars indicate the standard deviation between ten probability distributions derived independently from ten two-second exposures. Each distribution was fit to a Gaussian curve [green] using the 'fminsearch' function in MATLAB.

Fig. S9: Increase in variance with DNA length: published crystallographic, trsmFRET and DEER data. [A] Variance of the inter-strand separation distance between 3'-phosphates as measured by X-ray crystallography [squares] is plotted as a function of the number of intervening base-steps. A linear fit [blue dashed line, R^2=0.36] and a

quadratic fit [black solid line, R^2=0.35] give similar agreement with the data. [B] Variance of the inter-strand separation distance between fluorophores as measured by time-resolved single-molecule FRET (trsmFRET) experiments (*S4*) [circles] is plotted as a function of the number of intervening base-steps. A quadratic fit [black solid line, R^2=0.93] accounts better for the data than does a linear fit [blue dashed line, R^2=0.85]. The quadratic coefficient is 0.376 Å^2, indicating that the standard deviation of the distance measurements increases by ≈0.61 Å per base step. The y-intercept of the quadratic fit is 15.43 Å^2. [C] Variance of the inter-strand separation distance between nitroxide labels as measured by double electron-electron resonance (DEER) experiments (*S6*) [stars] is plotted as a function of the number of intervening base-steps. A quadratic fit [black solid line, R^2=0.96] accounts better for the data than does a linear fit [blue dashed line, R^2=0.90]. The quadratic coefficient is 0.25 Å^2, indicating that the standard deviation of the distance measurements increases by ≈0.5 Å per base step. The y-intercept of the quadratic fit is 3.62 Å^2.

Fig. S10: Individual probability distance distribution curves for the 10 [A], 15 [B], 20 [C], 25 [D], 30 [E], and 35 [F] base-pair duplexes. The distributions are normalized so that they sum to unity. Error bars indicate the standard deviation of ten probability distributions derived independently from ten one-second exposures. Each distribution was fit to a Gaussian curve [red] using the 'fminsearch' function in MATLAB.

Supplementary Figure S1:

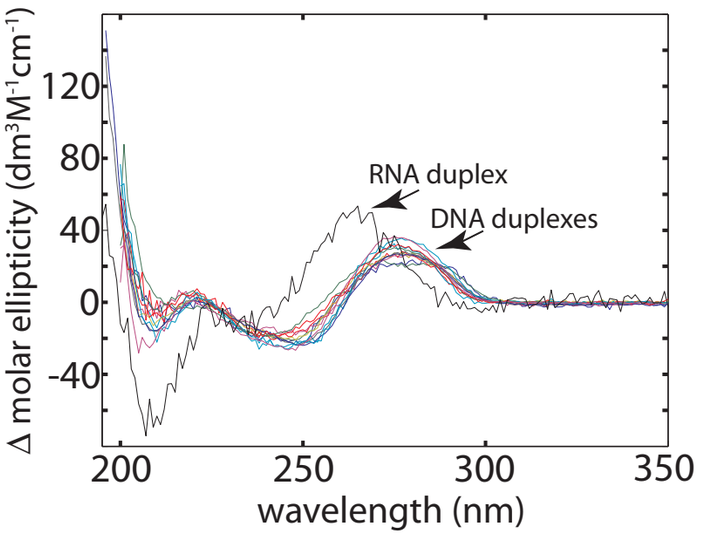

Supplementary Figure S2:

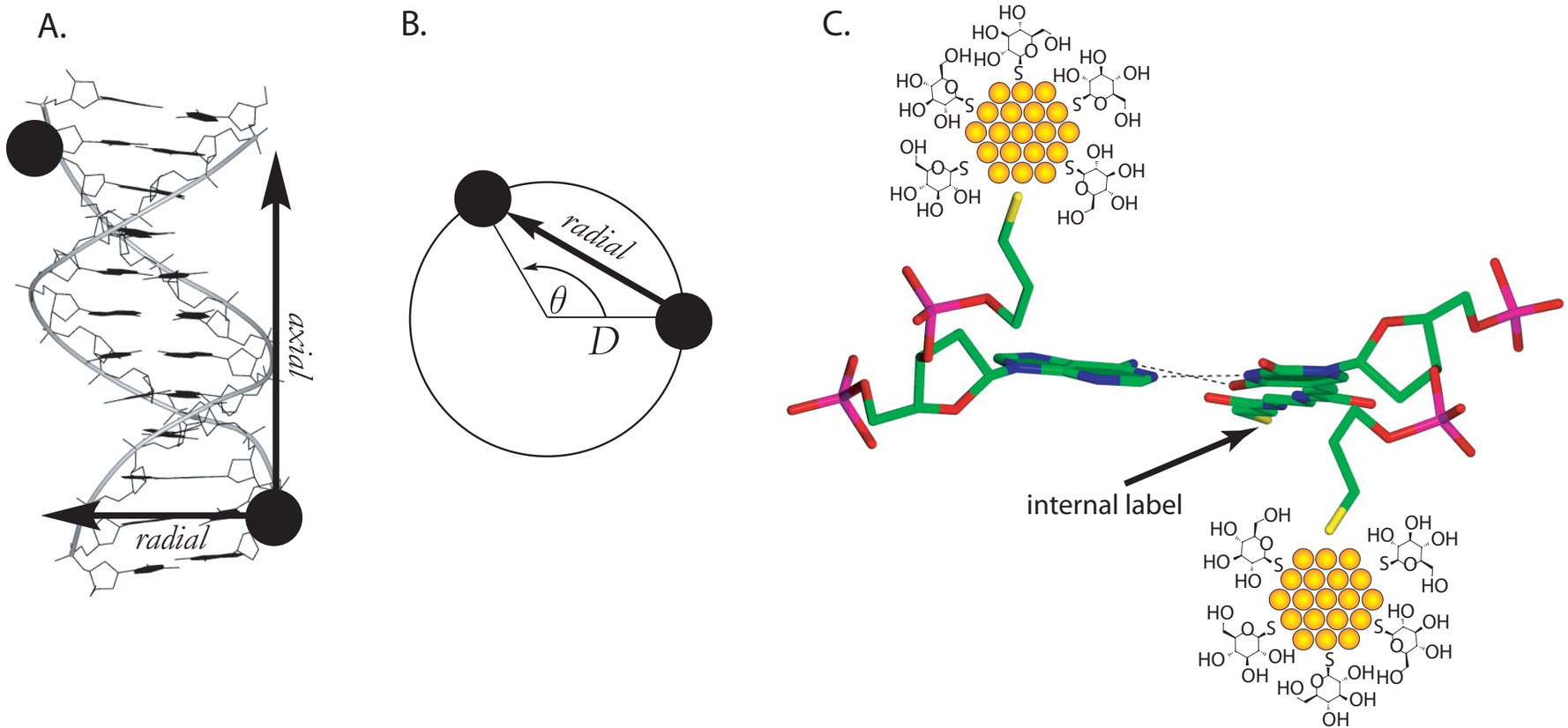

Supplementary Figure S3:

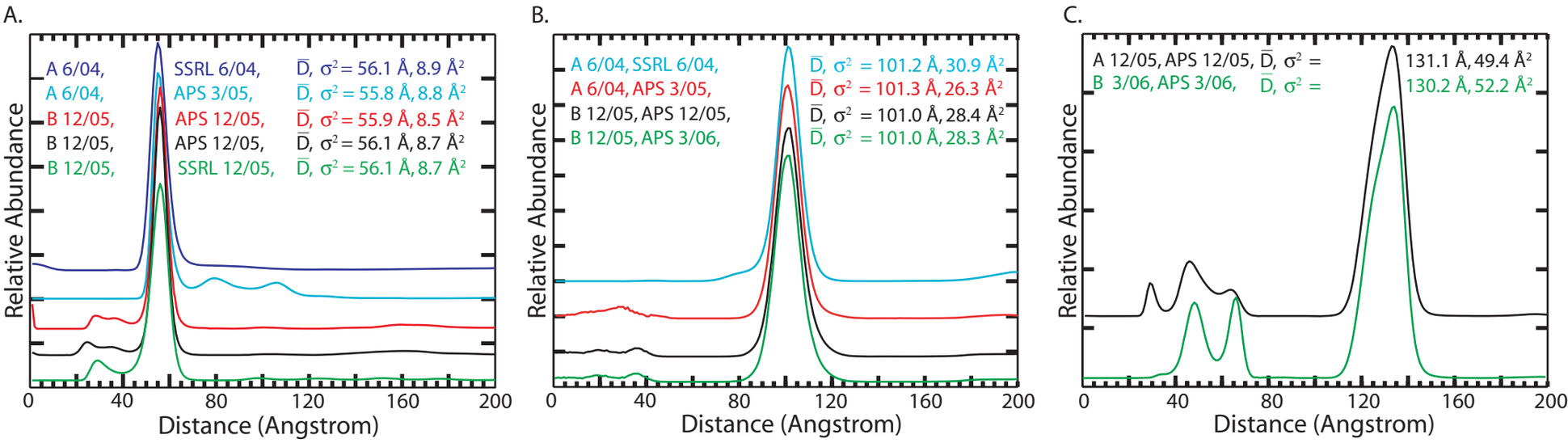

Supplementary Figure S4:

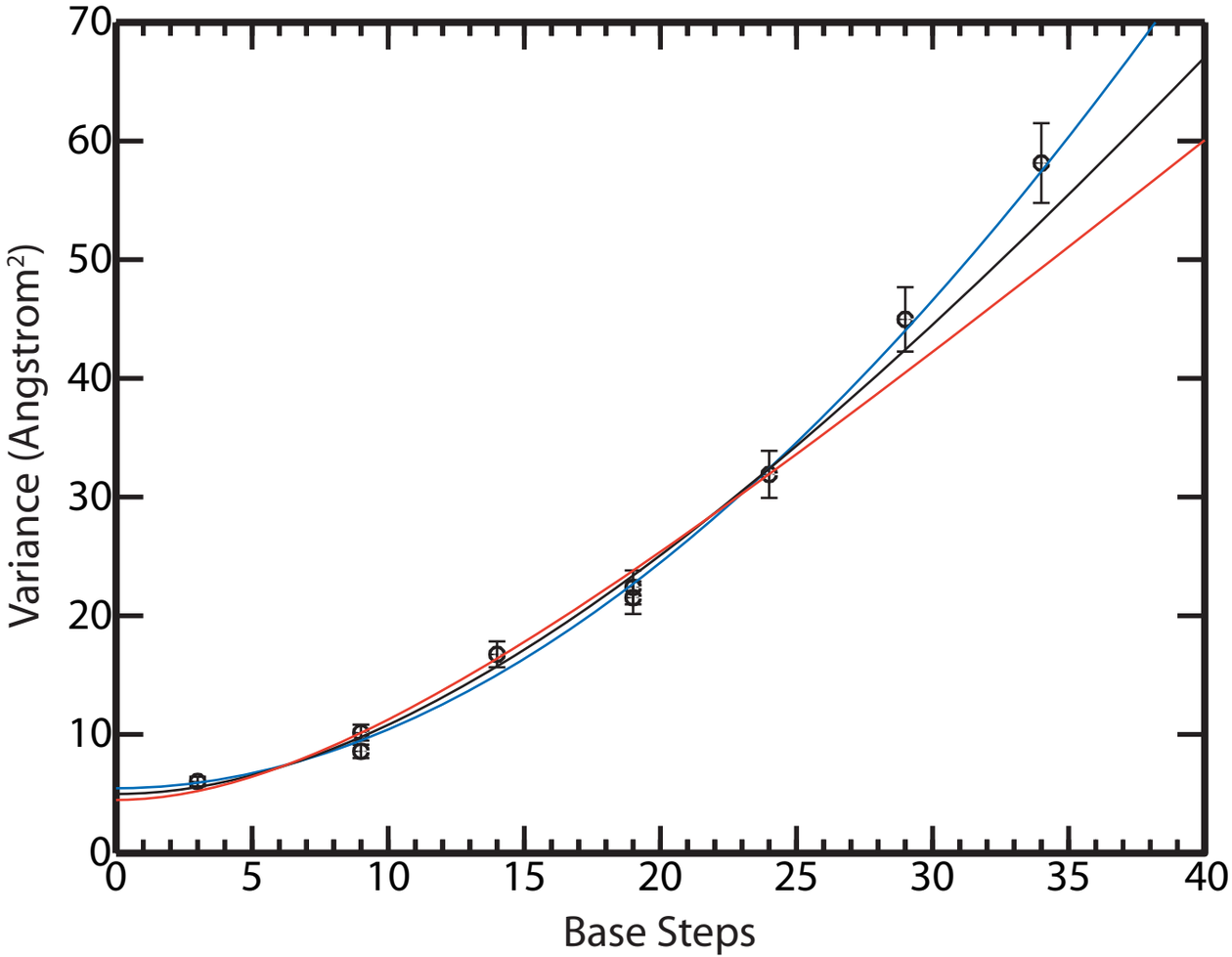

Supplementary Figure S5:

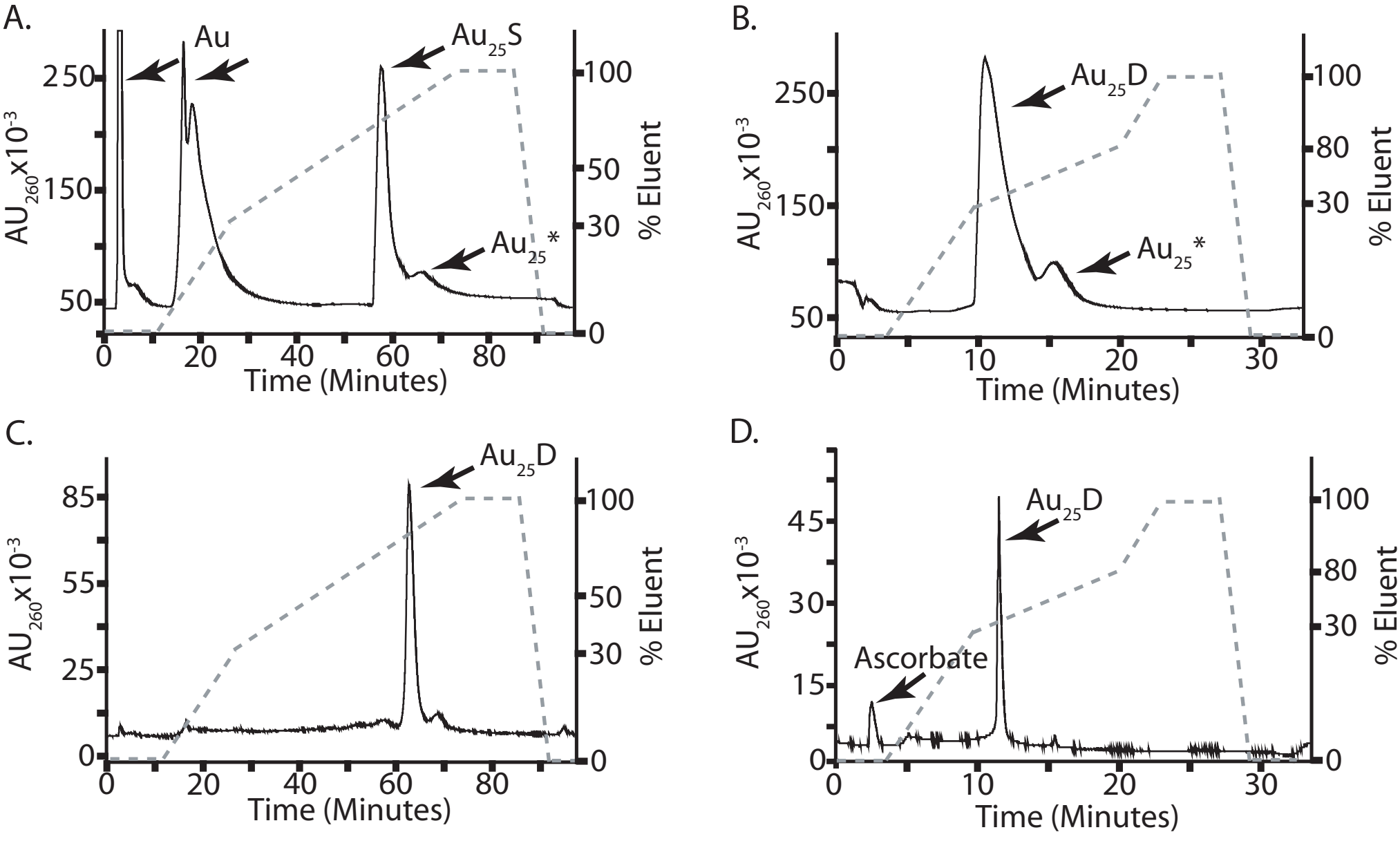

Supplementary Figure S6:

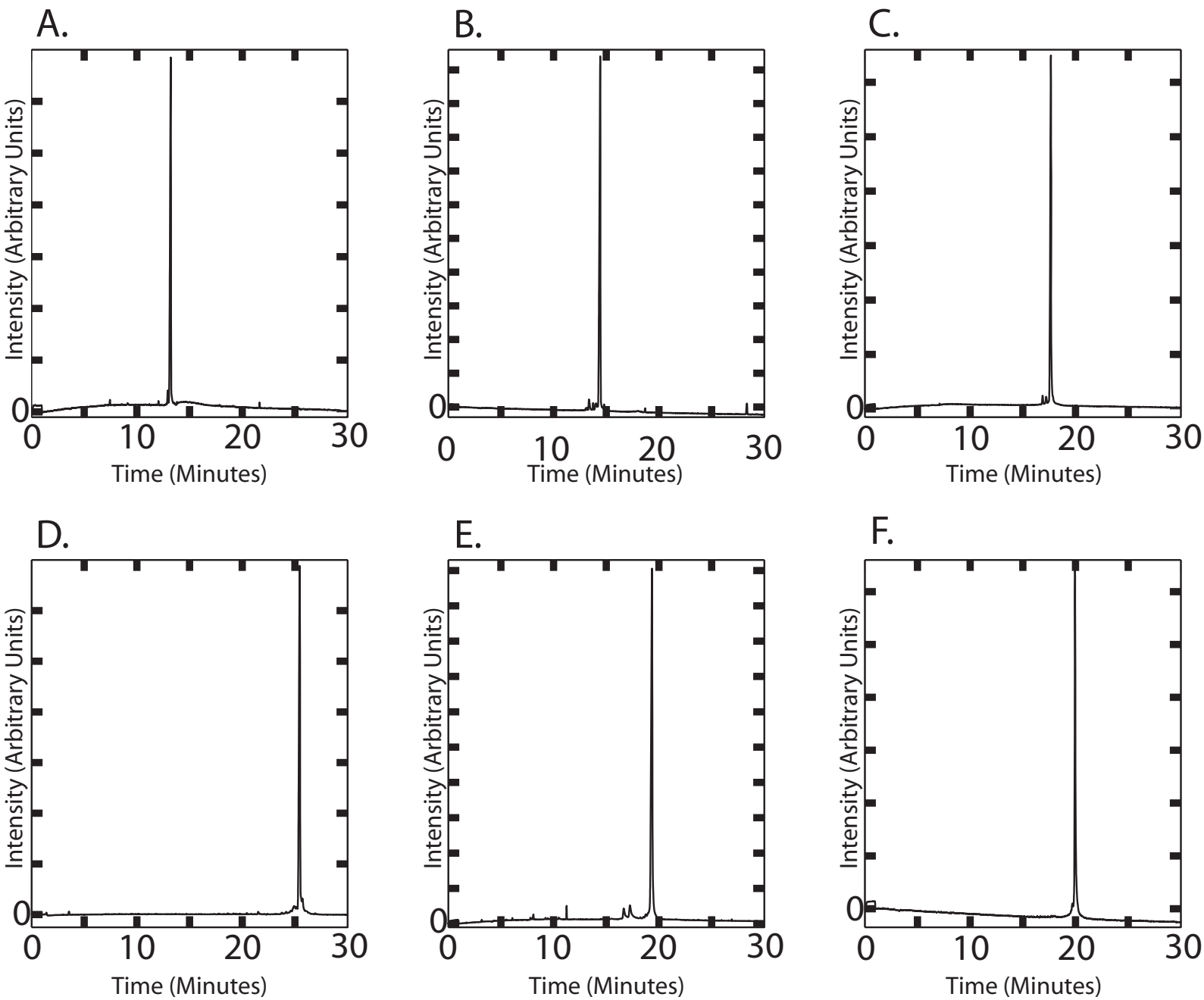

Supplementary Figure S7:

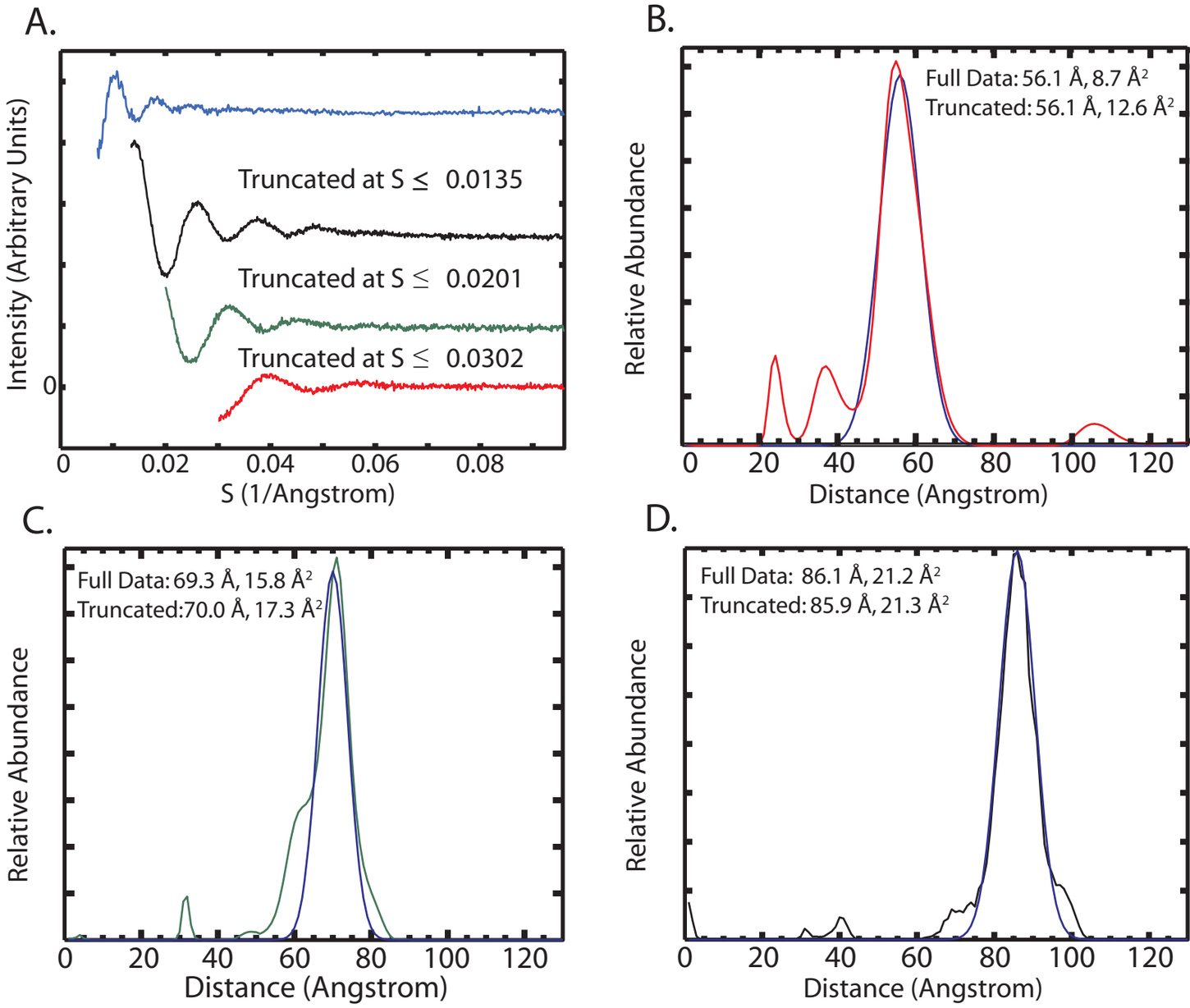

Supplementary Figure S8:

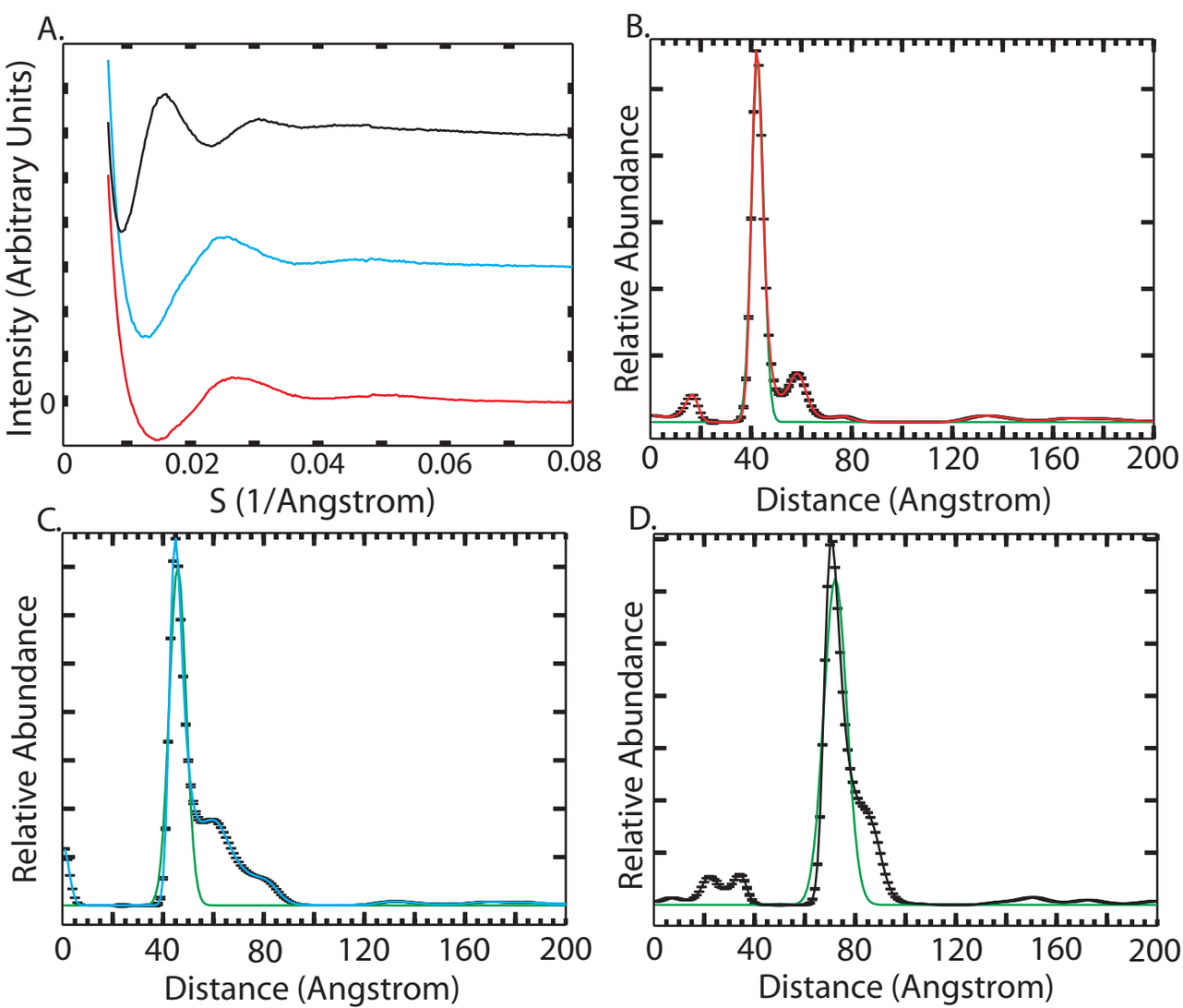

Supplementary Figure S9:

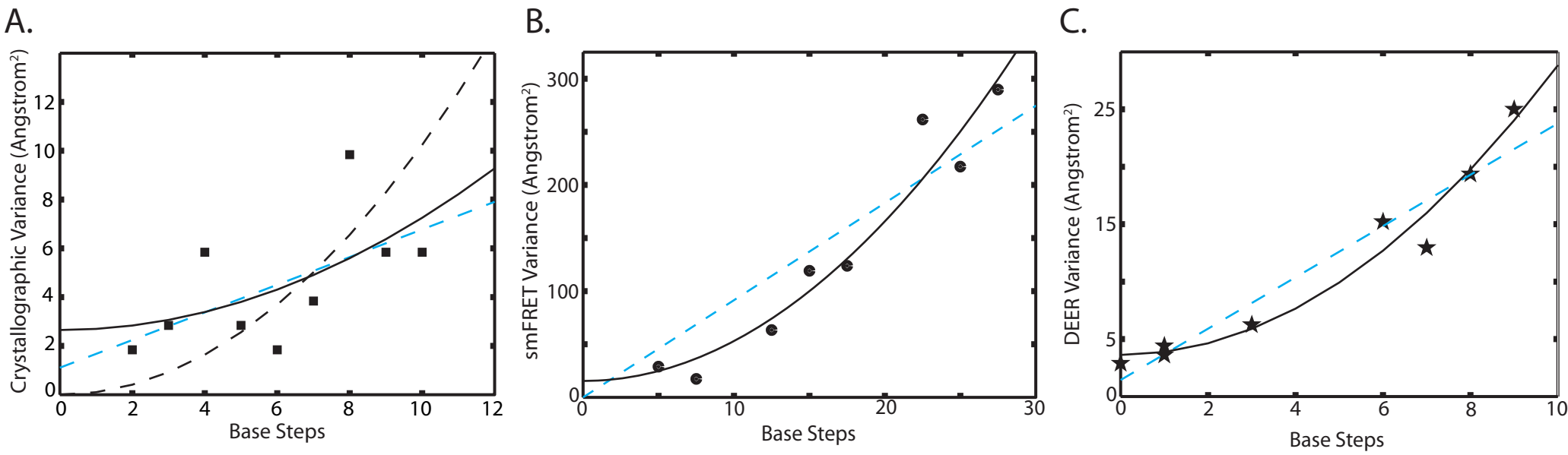

Supplementary Figure S10:

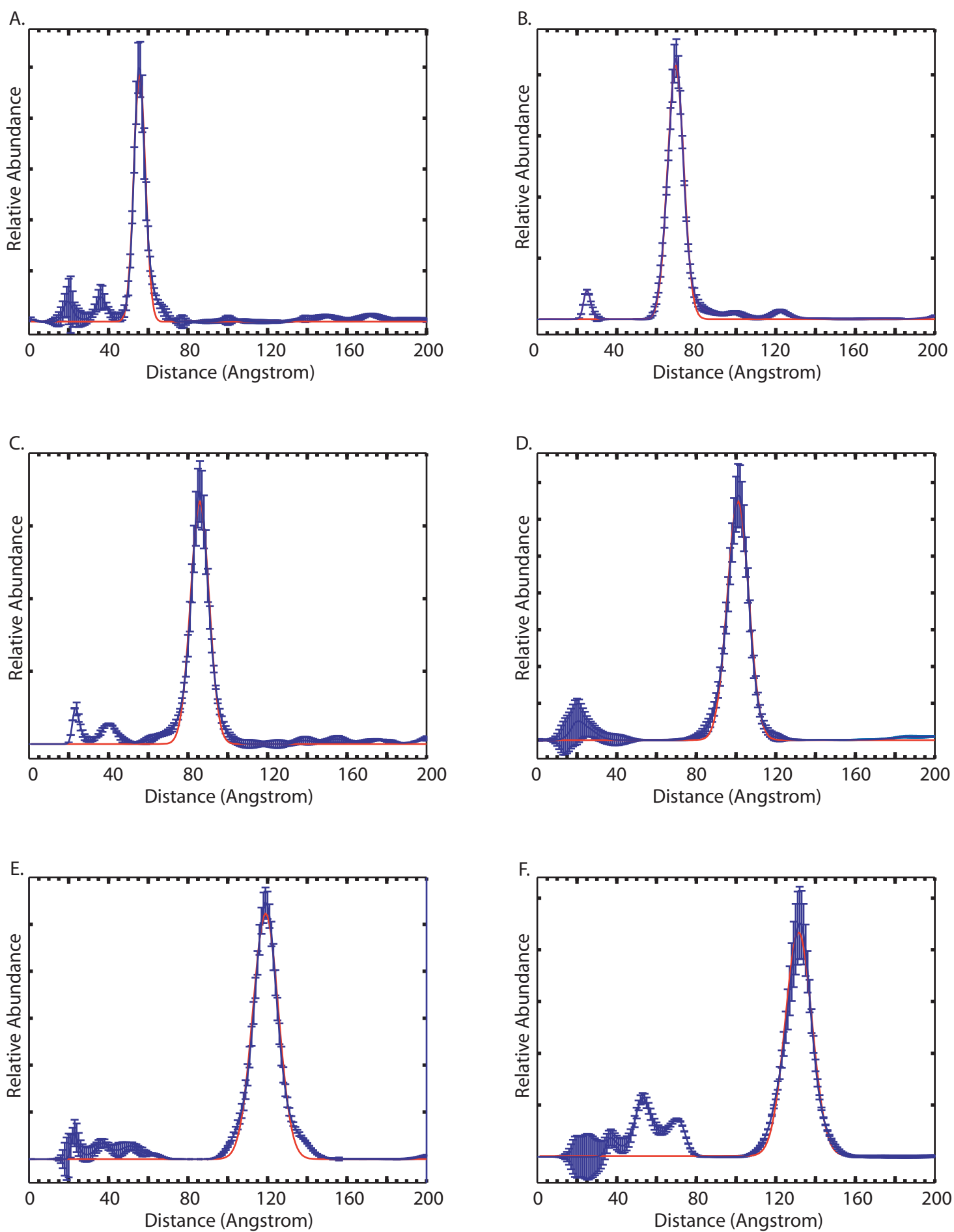

Table S1:

Number of Base Pairs	Unmodified (U) T_m (°C)	Double-Labeled (AB) T_m (°C)	ΔT_m (AB-U)	Single-Labeled (A) T_m (°C)	Single-Labeled (B) T_m (°C)	ΔT_m (A-U)	ΔT_m (AB-B)
10	45.0 ± 0.2	46.4 ± 0.1	+ 1.4	-	-	-	-
15	56.1 ± 0.3	58.1 ± 0.1	+ 2.0	-	-	-	-
20	65.0 ± 0.5	67.7 ± 0.2	+ 2.7	-	-	-	-
25	68.7 ± 0.3	70.0 ± 1.0	+ 1.3	69.4	69.6	+ 0.7	+ 0.4
30	73.5 ± 0.1	77.0 ± 1.0	+ 3.5	75.1	75.5	+ 1.6	+ 1.5
35	79.9 ± 0.6	81.7 ± 0.5	+ 1.8	80.9	80.9	+ 1.0	+ 0.8

Melting temperatures for unmodified, single-labeled and double-labeled DNA duplexes. The increase in melting temperature upon addition of the A nanocrystal is the same whether or not the B nanocrystal is present, indicating a zero coupling energy between the two nanocrystals. The samples were approximately 10 µM concentration in 1 M NaCl, 0.05 mM EDTA, and 10 mM sodium phosphate, pH 7.0. The reported error is the difference between three independent measurements.

Table S2:

Duplex Name		Sequence	Mean (Angstrom)	Variance (Angstrom^2)
10	A	5'-GCATCTGGGC-3'	55.7 ± 0.3	8.5 ± 0.6
	B	CGTAGACCCG		
15	A	5-CGACTCTACGGAAGG-3'	69.7 ± 0.4	16.5 ± 1.1
	B	GCTGAGATGCCTTCC		
20	A	5'-CGACTCTACGGCATCTGCGC-3'	86.0 ± 0.4	21.6 ± 1.4
	B	GCTGAGATGCCGTAGACGCG		
25	A	5'-CGACTCTACGGAAGGGCATCTGCGC-3'	101 ± 0.5	30.0 ± 2.0
	B	GCTGAGATGCCTTCCCGTAGACGCG		
30	A	5'-CGACTCTACGGAAGGTCTCGGACTACGCGC-3'	119.1 ± 0.6	41.1 ± 2.7
	B	GCTGAGATGCCTTCCAGAGCCTGATGCGCG		
35	A	5-CGACTCTACGGAAGGGCATCTCTCGGACTACGCGC-3'	131.3 ± 0.7	50.9 ± 3.4
	B	GCTGAGATGCCTTCCCGTAGAGAGCCTGATGCGCG		
Internal 3	A	5'- CGACTACGTACCGATGCATCACTACGCAGCGC-3'	43.0 ± 0.2	6.0 ± 0.4
	B	GCTGATGCATGGCTACGTAGTGATGCGTCGCG		
Internal 10	A	5'-GCACTACGTACCGATGCATCACTACGCAGCGC-3'	46.1 ± 0.2	10.1 ± 0.7
	B	CGTGATGCATGGCTACGTAGTGATGCGTCGCG		
Internal 20	A	5'- GCACTACGTACCGATGCATCACTACGCAGCGC-3'	75.2 ± 0.4	20.8 ± 1.4
	B	CGTGATGCATGGCTACGTAGTGATGCGTCGCG		

The sequences of the model DNA duplexes used in this study. Single strands are labeled A (sense) and B (antisense) for each DNA duplex. Oligonucleotides that were synthesized with the Glen Research 3'-Thiol Modifier (C3 S-S) were labeled at the 3' position. Oligonucleotides that were synthesized with the Glen Research amino C2 dT modifier were labeled at internal T base positions (red). Mean gold-gold separation distances and variances are reported as a function of length for each DNA duplex. The uncertainties in the mean and variance estimates are assumed to be ± 0.5% and ± 6.6% respectively, based on the standard deviation of repeated measurements for the 10, 25 and 35 base-pair duplexes (Fig. S3).

Table S3:

L_0 (b.p.)	L_0	ΔL [a]	ΔL [b]	ΔL^2_{rms} [a]	ΔL^2_{rms} [b]
10	33 Å	–0.3 Å	–0.3 Å	+0.05 Å^2	+0.04 Å^2
15	49 Å	–0.8 Å	–0.8 Å	+0.23 Å^2	+0.24 Å^2
20	65 Å	–1.4 Å	–1.4 Å	+0.73 Å^2	+0.77 Å^2
25	81 Å	–2.1 Å	–2.2 Å	+1.71 Å^2	+1.88 Å^2
30	98 Å	–3.0 Å	–3.1 Å	+3.41 Å^2	+3.89 Å^2
35	114 Å	–4.1 Å	–4.2 Å	+6.69 Å^2	+7.22 Å^2

[a] Values from Monte Carlo simulations with 40 subelements of the worm-like chain.
[b] Values using the analytical formula of Schurr and Fujimoto (*S7*).

Expected effects of bending fluctuations on the end-to-end distance distributions of rods with contour lengths L_0 corresponding to the duplexes probed in this study, calculated with Monte Carlo simulations and an analytical formula (*S7*). The bending persistence length was assumed to be P = 511 Å, as observed in single molecule force experiments under similar ionic conditions (*S8*). To avoid bias, values for the reduction in mean end-to-end length (ΔL) and variance of end-to-end length (ΔL^2_{rms}) were calculated assuming rise per base pair values of 3.1 Å, 3.25 Å, and 3.4 Å. The results with 3.1 Å and 3.4 Å rise per base pair values were within 10% (for ΔL) and 20% (for ΔL^2_{rms}) of the results with 3.25 Å rise per base pair; the latter results are presented. For all parameters tested, the Monte Carlo calculations and the analytical formula gave similar results, as shown.

Table S4:

NDB CODE	length	PDB CODE
BDF068	6	251D
BDH071-1	8	250D
BDH071-2	8	250D
BDH071-3	8	250D
BDJ008	10	3DNB
BDJ017	10	1BD1
BDJ019	10	5DNB
BDJ025	10	1D23
BDJ031	10	1D49
BDJ036	10	1D56
BDJ037	10	1D57
BDJ039	10	1CGC
BDJ051	10	126D
BDJ052	10	158D
BDJ055	10	167D
BDJ060	10	196D
BDJ061	10	N/A
BDJ069	10	252D
BDJ081-1	10	307D
BDJ081-2	10	307D
BDJ081-3	10	307D
BDJB27	10	2D25
BDJB43	10	1D60
BDJB44	10	1D61
BDJB48	10	1DA3
BDJB57	10	183D
BDL005	12	7BNA
BDL011	12	1D99
BDL012	12	112D
BDL014	12	111D
BDL015-1	12	1BDN
BDL015-2	12	1BDN
BDL022	12	1DNM
BDL028	12	1D28
BDL029	12	1D29
BDL038	12	1D65
BDL042	12	119D
BDL046	12	1D80
BDL047-1	12	1D89
BDL047-2	12	1D89
BDL047-3	12	1D89
BDL059	12	194D
BDL070-1	12	249D

NDB CODE	length	PDB CODE
BDL070-2	12	249D
BDL075	12	271D
BDL078	12	287D
BDLB03	12	3BNA
BDLB04	12	4BNA
BDLB10	12	114D
BDLB13	12	4DNB
BDLB26	12	1D27
BDLB33	12	1D75
BDLB40	12	1D77
BDLB41	12	1D81
BDLB53	12	153D
BDLB54	12	150D
BDLB56	12	178D
BDLB58	12	218D
BDLB72	12	265D
BDLB73	12	266D
BDLB74	12	270D
BDLB76	12	285D
BDLB82	12	297D
BD0093	6	2G1Z
BD0039	6	1F69
BD0040	6	1F6C
BD0050	6	1IH1
BD0063	6	1P24
BD0064	6	1P25
BD0065	6	1P26
BDF062	6	206D
BDFP24	6	1D97
DD0056	6	1P20
BD0069	7	1S9B
BD0088	8	2A2T
BD0037	9	1ENN
UDI030	9	208D
UDI047	9	253D
BD0028	10	1DCV
BD0055	10	1D62
BD0059	10	1N4E
BD0073	10	1WQY
BD0079	10	1ZF5
BD0082	10	1ZFC
BD0083	10	1ZFE
BD0084	10	1ZFG
BD0085	10	1ZFH
BD0086	10	1ZFM

NDB CODE	length	PDB CODE
BD0087	10	1ZFF
BDJB77	10	286D
UDJ031	10	237D
UDJ049	10	272D
UDJ060	10	309D
BD0012	10	460D
BD0013	10	461D
BD0015	10	1QC1
BD0021	10	1CW9
BD0023	10	1D8G
BD0024	10	1D8X
BD0025	10	1D9R
BD0027	10	1DCR
BD0033	10	1EN3
BD0034	10	1EN8
BD0035	10	1EN9
BD0036	10	1ENE
BD0042	10	1G3V
BD0051	10	1IKK
UD0053	10	1SM5
BD0066	10	1S23
BD0068	10	1S1K
BD0071	10	1SK5
BD0076	10	1ZEW
BD0077	10	1ZF0
BD0080	10	1ZF7
BD0081	10	1ZFB
BDJB49	10	122D
BDJB50	10	123D
UD0004	10	446D
UD0012	10	1G6D
UD0023	10	1NQS
UD0024	10	1NT8
UD0025	10	1NVN
UD0026	10	1NVY
UD0028	10	1P4Y
UD0029	10	1P4Z
UD0030	10	1P54
UDJ061	10	335D
BD0018	11	476D
BD0056	11	1K71
BD0002	12	424D
BD0003	12	425D
BD0032	12	1EHV
BD0047	12	1HQ7

NDB CODE	length	PDB CODE
BD0052	12	1ILC
BD0089	12	2AF1
BDL001	12	1BNA
BDL002	12	2BNA
BDL006	12	1D98
BDL007	12	1DN9
BDL009	12	113D
BDL018	12	N/A
BDL020	12	9BNA
BDL021	12	N/A
BDL035	12	330D
BD0001	12	423D
BD0004	12	426D
BD0005	12	428D
BD0007	12	436D
BD0008	12	455D
BD0009	12	456D
BD0010	12	457D
BD0011	12	458D
BD0014	12	463D
BD0019	12	477D
BD0020	12	478D
BD0022	12	1QP5
BD0029	12	1DOU
BD0030	12	1DPN
BD0031	12	1EDR
BD0038	12	1EI4
BD0041	12	1FQ2
BD0043	12	1G75
BD0044	12	1G8N
BD0045	12	1G8U
BD0046	12	1G8V
BD0048	12	1I3T
BD0049	12	1I47
BD0053	12	1J8L
BD0054	12	1JGR
BD0057	12	1LP7
BD0060	12	1N1O
BD0061	12	1N5C
BD0062	12	1NGT
BD0067	12	1S2R
BD0072	12	1VE8
BD0075	12	1Z5T
BD0090	12	2B1D
BD0091	12	2FIH

NDB CODE	length	PDB CODE
BD0092	12	2FII
BDL032	12	1NDN
BDL084	12	355D
BDLB83	12	329D
BDLB84	12	388D
BDLB85	12	389D
BDLS67	12	233D
BDLS79	12	290D
BDLS80	12	291D
DD0059	12	1QV4
UDM010	13	1D31
BD0070	17	1SGS

RED = CODES FROM OLSON STUDY (*S2*)
BLACK = CODES FROM ALL OTHER SEQUENCES THAT WERE PUBLISHED AFTER OLSON STUDY

PDB codes for the crystallographic coordinates of B-form DNA used to calculate end-to-end distance variance.

References and Notes:

S1. R. S. Mathew-Fenn, R. Das, J.A. Silverman, P.A. Walker, P.B. Harbury, *submitted* (2008).

S2. W. K. Olson, A. A. Gorin, X. J. Lu, L. M. Hock, V. B. Zhurkin, *Proc. Natl. Acad. Sci. USA* **95**, 11163 (1998).

S3. H. M. Berman *et al.*, *Biophys. J.* **63,** 751 (1992).

S4. T. A. Laurence, X. Kong, M. Jager, S. Weiss, *Proc. Natl. Acad. Sci. USA* **102,** 17348 (2005).

S5. T. D. Fenn, D. Ringe, G. A. Petsko, *J. Appl. Cryst.* **36,** 944 (2003)

S6. Q. Cai *et al.*, *Nucleic Acids Res.* **34,** 4722 (2006).

S7. B. S. Fujimoto, J. M. Schurr, *Biopolymers* **54**, 561 (2000).

S8. C. G. Baumann, S. B. Smith, V. A. Bloomfield, C. Bustamante, *Proc. Natl. Acad. Sci. USA* **94**, 6185 (1997).

References and Notes:

S1. R. S. Mathew-Fenn, R. Das, J.A. Silverman, P.A. Walker, P.B. Harbury, *submitted* (2008).

S2. W. K. Olson, A. A. Gorin, X. J. Lu, L. M. Hock, V. B. Zhurkin, *Proc. Natl. Acad. Sci. USA* **95**, 11163 (1998).

S3. H. M. Berman *et al.*, *Biophys. J.* **63,** 751 (1992).

S4. T. A. Laurence, X. Kong, M. Jager, S. Weiss, *Proc. Natl. Acad. Sci. USA* **102,** 17348 (2005).

S5. T. D. Fenn, D. Ringe, G. A. Petsko, *J. Appl. Cryst.* **36,** 944 (2003)

S6. Q. Cai *et al.*, *Nucleic Acids Res.* **34,** 4722 (2006).

S7. B. S. Fujimoto, J. M. Schurr, *Biopolymers* **54**, 561 (2000).

S8. C. G. Baumann, S. B. Smith, V. A. Bloomfield, C. Bustamante, *Proc. Natl. Acad. Sci. USA* **94**, 6185 (1997).